PHYSICAL REVIEW B **98**, 104402 (2018)

Twisted domain walls and skyrmions in perpendicularly magnetized multilayers

Ivan Lemesh[*] and Geoffrey S. D. Beach

Department of Materials Science and Engineering, Massachusetts Institute of Technology, Cambridge, Massachusetts 02139, USA

(Received 28 June 2018; published 4 September 2018)

We present an analytical theory to describe three-dimensional magnetic textures in perpendicularly magnetized magnetic multilayers that arise in the presence of magnetostatic interactions and the Dzyaloshinskii-Moriya interaction (DMI). We demonstrate that domain walls in multilayers develop a complex twisted structure, which persists even for films with strong DMI. The origin of this twist is surface-volume stray field interactions that manifest as a depth-dependent effective field whose form mimics the DMI effective field. We find that the wall twist has a minor impact on the equilibrium skyrmion or domain size but can significantly affect current-driven dynamics. Our conclusions are based on the derived analytical expressions for the magnetostatic energy and confirmed by micromagnetic simulations.

DOI: 10.1103/PhysRevB.98.104402

I. INTRODUCTION

Magnetic thin films with chiral exchange interactions can host a variety of topological spin textures such as homochiral domain walls (DWs) [1–3] and magnetic skyrmions [4–6] with rich fundamental behaviors. Although usually considered as two-dimensional (2D) systems, thin films with competing surface and volume interactions can exhibit more complex three-dimensional (3D) textures, as recently realized in the case of cubic helimagnets [7–12] with bulk Dzyaloshinskii-Moriya interaction (DMI). In the case of heavy-metal/ferromagnet bilayers with perpendicular magnetic anisotropy (PMA) and interfacial DMI, the ferromagnet thickness is typically much less than the exchange length so the spin textures are truly 2D [13–15]. However, recent efforts to stabilize such textures at room temperature have employed multilayers in which the 2D textures are coupled from layer to layer by dipolar fields [15–20]. Such composite spin textures are usually treated two dimensionally with magnetic properties scaled using an effective medium approach [17,21,22] and with the assumption of a layer-independent magnetization profile (the 2D model). However, recently [23,24], it has been argued that the actual magnetic configuration of multilayers is rather different, and that the equilibrium DW width Δ and angle ψ vary from one layer to another. Previously, such an idea of twisted DWs has already been explored theoretically by Schlömann [25,26], who found a similar magnetization distribution in thick magnetic single layer films ($\mathcal{T} > l_{ex}$).

In this paper, we show DW twists [see Fig. 1(a)] emerge as a general feature in magnetic thin film multilayers due to chiral stray field interactions. We solve the multilayer stray field integrals analytically and find that the twist is caused by the previously ignored mutual surface-volume stray field interactions, which mathematically resemble a layer-dependent interfacial Dzyaloshinskii-Moriya interaction (DMI). We develop an analytical 3D model to accurately predict the equilibrium structure of domains and skyrmions, as well as to describe current-driven skyrmion dynamics.

II. TWISTED STRAIGHT DOMAIN WALL

First, consider an isolated straight DW in a multilayer film comprised of magnetic and nonmagnetic layers, where $\mathcal{T}$ is the magnetic layer thickness, $\mathcal{P}$ is the multilayer period, and $\mathcal{N}$ is the number of multilayer repeats. Micromagnetic simulations for a representative Co-based multilayer [15–20] (saturation magnetization $M_s = 1.4 \times 10^6$ A/m, exchange stiffness $A = 1.0 \times 10^{-11}$ J/m, quality factor $Q = 2K_u/(\mu_0 M_s^2) = 1.4$, and with $\mathcal{N} = 15$, $\mathcal{T} = 1$ nm and, $\mathcal{P} = 6$ nm), summarized in Figs. 1(a)–1(d), reveal that both Δ_i and the DW angle ψ_i varies from layer to layer (i). When the DMI constant $D = 0$, the DWs in the top and the bottom layers have Néel profiles with opposite chiralities and larger Δ. In contrast, the middle layers exhibit Bloch DWs with smaller Δ. Increasing the DMI shifts the position of the Bloch layer towards one surface, and at very high DMI all the layers saturate to a homochiral Néel state.

Figure 2(a) shows schematically the stray fields around the Bloch layer (i_{Bloch}), explaining the origin of the wall twist. In the adjacent top and bottom nonmagnetic layers, the surface stray fields of the neighboring domains are antiparallel. The energy of the system is minimized if these fields are coaligned with the stray fields from the neighboring layers, giving rise to domain coupling. This tendency also favors the creation of corresponding volume charges $\rho_v = -\nabla \cdot \mathbf{M}$ (shown in blue), which results in the observed DW twist. The stray fields tend to increase (decrease) Δ when they are parallel (antiparallel) to the DW magnetization, hence leading to the observed thickness-dependent Δ.

To quantify these effects, one must calculate the corresponding surface-volume stray field integral [27]

$$\sigma_{d,sv}^{1,\mathcal{N}} = \frac{\mu_0}{4\pi \mathcal{N} \mathcal{P} L_y} \iint \mathrm{d}^3 r \, \mathrm{d}^3 r' \rho_s(\mathbf{r}) \frac{1}{|\mathbf{r} - \mathbf{r}'|} \rho_v(\mathbf{r}'). \qquad (1)$$

We assume that the DW in each layer i can be described by its wall angle ψ_i and polar angle (θ) through

---

[*] ivan.g.lemesh@gmail.com

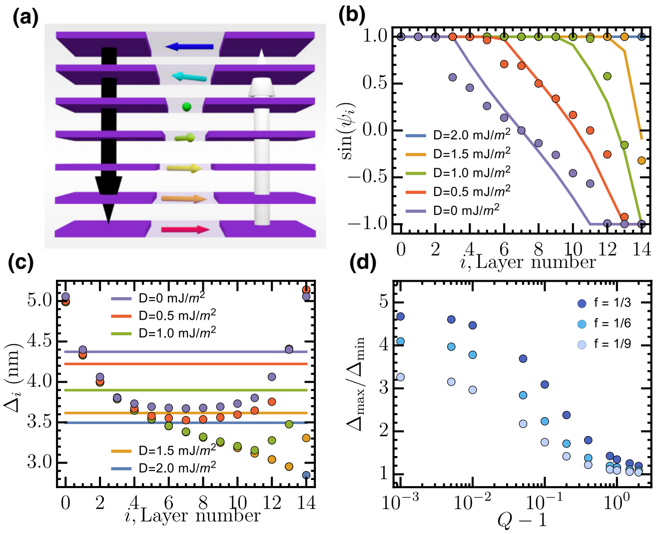

FIG. 1. DW twist. (a) Schematic plot of the (↓ | ↑) twisted DW. (b) ψ_i and (c) Δ_i as a function of the layer number and interfacial DMI for a film with $Q = 1.4$. Points represent the simulated results; continuous lines show the numerical solution of the proposed twisted wall theory. (d) $\Delta_{\max}/\Delta_{\min}$ ratio as a function of Q and scaling factor $f = \mathcal{T}/\mathcal{P}$.

$\theta_i(x) = \arctan\{\exp[\mp(x-q)/\Delta_i]\}$ [28], where upper (lower) sign stands for ↓ | ↑ (↑ | ↓) DW state. Micromagnetic simulations indicate that ψ_i also varies as a function of coordinate [29], $\psi_i = \psi_i(x)$ (see Supplemental Material [30]). However, this effect occurs dominantly in the tails of the DW, and we therefore neglect it in our analytical model. For the purpose of comparison between micromagnetic simulations and our analytical model, we fitted all the simulation data with this simplified DW profile, in which case the fitted ψ_i are dominated by the region near the DW center.

As shown in the Supplemental Material [30], Eq. (1) for an infinitely extended film ($L_x, L_y \to \infty$) reduces to

$$\sigma_{d,sv}^{1,\mathcal{N}} = \mp\frac{\pi f}{\mathcal{N}}\sum_{i=0}^{\mathcal{N}-1}\sin(\psi_i)D_{sv,i}(\Delta_0, \ldots, \Delta_{\mathcal{N}-1}) \tag{2}$$

with $f = \mathcal{T}/\mathcal{P}$ being a scaling factor. A key result is that this expression follows the exact functional form of a (layer-dependent) interfacial DMI. That is, surface-volume stray fields manifest as a chiral magnetostatic interaction that promotes homochiral textures within each individual layer, even in the absence of DMI. The twist develops as a consequence of the fact that $D_{sv,i}$ is an asymmetric function with respect to i, ranging from zero at the middle layer to its maximum magnitude at the top and the bottom layers [with the opposite signs, as depicted in Fig. 2(b)]. Adding interfacial DMI simply offsets $D_{sv,i}$ by D in every layer, which leads to a net shift of the Bloch layer away from the center.

Since the $D_{sv,i}$ each depend on every Δ_j, the coupled magnetostatic integrals in Eq. (2) involve $2\mathcal{N}$ independent variables, Δ_i, ψ_i, leading to analytically intractable magnetostatic integrals [see Eq. (A1)]. However, micromagnetic simulations [Fig. 1(d)] reveal that $\Delta_{\max}/\Delta_{\min}$ differs significantly from 1 only for relatively low Q. We henceforth treat Δ as constant across the layers, which allows for analytical solutions for the ψ_i to be obtained. The total magnetostatic energy of the isolated DW (including volume-volume, surface-surface, and surface-volume components) can then be reduced to

$$\begin{aligned}\sigma_d^{1,\mathcal{N}}&(\Delta, \psi_i)\\ &= \sum_{i=0}^{\mathcal{N}-1}\sum_{j=0}^{\mathcal{N}-1}\{\sin(\psi_i)\sin(\psi_j)F_{v,ij}(\Delta)\\ &\quad + F_{s,ij}(\Delta) \pm \sin(\psi_i)\mathrm{sgn}(i-j)F_{sv,ij}(\Delta)\}\end{aligned} \tag{3}$$

with functions $F_{\alpha,ij}$ derived in the Supplemental Material [30] and defined analytically in Eq. (A2). Here, we treat the layered structure explicitly rather than through the effective medium approximation [17,21], as we find that the intrinsic error of that approach affects the prediction accuracy of Δ, ψ_i (and more importantly, the sizes of domains and skyrmions [22]). The total micromagnetic energy $\sigma_{\text{tot}}^{1,\mathcal{N}}(\Delta, \psi_i)$ then reads

$$\sigma_{\text{tot}}^{1,\mathcal{N}} = \sigma_d^{1,\mathcal{N}} + \frac{2A}{\Delta}f + 2K_u\Delta f \mp \frac{\pi D f}{\mathcal{N}}\sum_{i=0}^{\mathcal{N}-1}\sin(\psi_i). \tag{4}$$

The equilibrium profile is obtained by setting $\frac{\partial\sigma_{\text{tot}}^{1,\mathcal{N}}}{\partial\Delta} = 0$, $\frac{\partial\sigma_{\text{tot}}^{1,\mathcal{N}}}{\partial\psi_i} = 0$ for $i = 0, \ldots \mathcal{N}-1$, which after introducing the matrix formalism (shown in the Supplemental Material [30]) reduces to

$$\begin{aligned}\frac{2A}{\Delta^2}&f - 2K_u f\\ &= \mp\frac{\pi f}{\mathcal{N}}\sum_{i=0}^{\mathcal{N}-1}\sin(\psi_i)\frac{\partial D_{sv,i}}{\partial\Delta}\\ &\quad + \sum_{i=0}^{\mathcal{N}-1}\sum_{j=0}^{\mathcal{N}-1}\left\{\frac{\partial F_{s,ij}}{\partial\Delta} + \sin(\psi_i)\sin(\psi_j)\frac{\partial F_{v,ij}}{\partial\Delta}\right\},\end{aligned} \tag{5}$$

$$\sin(\psi_i) = \pm\tilde{f}\left(\frac{\pi f}{\mathcal{N}}\hat{\varkappa}_v^{-1}\cdot[\vec{D}_{sv} + \vec{1}D]\right)_i, \tag{6}$$

where we introduced a helper function $\tilde{f}(x)$ that becomes x, when $|x| \leqslant 1$ and $\mathrm{sgn}(x)$ otherwise, and defined the matrix $\hat{\varkappa}_v$ and vector $\vec{D}_{sv}$ as:

$$\varkappa_{v,ij} = (1+\delta_{ij})F_{v,ij}(\Delta) \tag{7}$$

$$D_{sv,i} = -\frac{\mathcal{N}}{\pi f}\sum_{j=0}^{\mathcal{N}-1}F_{sv,ij}(\Delta)\mathrm{sgn}(i-j). \tag{8}$$

Equations (5) and (6) constitute an implicit relation for the equilibrium Δ, which can be disentangled from $\sin(\psi_i)$ through separation of variables. The equilibrium ψ_i can then be found by plugging the obtained Δ directly into Eq. (6). The resulting analytical solutions of Δ, ψ_i for films with various D are plotted in Figs. 1(b) and 1(c). We find that Δ in our model correctly predicts the average DW width $\sum_0^{\mathcal{N}-1}\Delta_i/\mathcal{N}$, and our constant Δ approximation permits quite accurate prediction of the layer-dependent ψ_i (even when $\Delta_{\max}/\Delta_{\min} \sim 4$ as shown for a film with $Q = 1.01$, $f = 1/6$ in Supplemental Fig. 1 [30]).

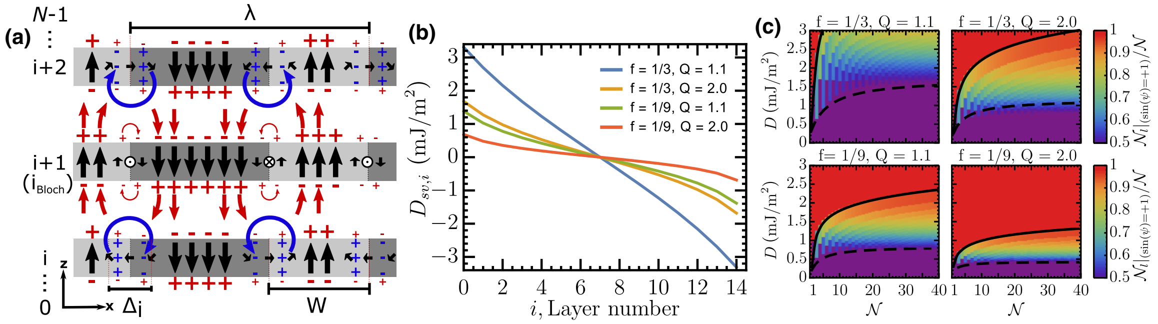

FIG. 2. DW twist. (a) The schematic distribution of the surface (volume) charges depicted with red (blue) signs in the layers surrounding the Bloch layer. (b) The surface-volume stray field interaction term D_{sv} as a function of the layer number i, for various values of f and Q for $(\downarrow \mid \uparrow)$ twisted DW. (c) The fraction of layers with $\sin(\psi_i) = +1$ as a function of DMI, $\mathcal{N}$, f, and Q. The dashed curves in (c) correspond to the 2D model prediction of the threshold for purely Néel DWs. The solid curves give the 3D analytical model prediction derived here.

We find that the values of D_{sv} in typical multilayers are comparable to values of interfacial DMI found experimentally, as shown in Fig. 2(b), where energies on the order of 1 mJ/m^2 are seen. Its magnitude increases with increasing f and decreasing Q. Figure 2(c) shows that as a result, much larger values of DMI are required to saturate DWs in a purely Néel state than would be expected from a 2D treatment. There, we analyze multilayers with various Q and f and plot the fraction of layers with right-handed Néel walls [here, $\sin(\psi_i) = +1$] as a function of DMI and $\mathcal{N}$. We find that films with the smallest f and Q are easier to saturate to the complete Néel state. We also find that the threshold $D^{2D}_{\text{thr.}}$, at which the wall in every layer becomes completely Néel in the 2D model, [22,31] applied to multilayers using an effective medium approach [Eq. (A8)], [dashed curve in Fig. 2(c)] significantly underestimates the actual threshold. In the Supplemental Material [30] we derive a more precise numerical relation for $D^{3D}_{\text{thr.}}$ [Eqs. (A6) and (A7)], plotted as continuous curves in Fig. 2(c). Notably, we find that the critical DMI strength required to ensure uniform Néel character is more than a factor of 2 greater than would be estimated from a 2D treatment. We note that an analytical treatment to determine the threshold for the onset of a twist was also presented recently in Ref. [29].

One can see from the form of Eq. (6) that volume-volume stray fields, accounted for by $\hat{\varkappa}_v^{-1}$, also influence the layer dependent ψ_i. However, if D_{sv} is neglected, the volume-volume interactions alone would predict a twist only in the case of nonzero DMI and that twist would be symmetric, since the matrix $\hat{\varkappa}_v^{-1}$ is centrosymmetric (see Supplemental Material [30]). It is, in fact, the surface-volume stray fields that lead to the experimentally observed asymmetric twist [23,24,29], since the vector D_{sv} in Eq. (6) is antisymmetric.

III. DOMAIN SIZE

We now consider a multidomain state with twisted DWs, with domain period λ and minority domain width W. One can anticipate that shifting from the 2D model to the 3D model should result in first-order corrections to the intra- and interwall energetics of the system, which would lead to more accurate predictions of W [17,22]. To evaluate the impact of this effect, we first identified the ground state for multilayer films with low DMI using micromagnetic simulations with various densities of stripes. After performing a relaxation procedure [22], we find that the state with minimum total energy is the one in which the intralayer DW chirality is conserved. This effect is also induced by the surface-volume stray field interactions as depicted in Fig. 2(a).

Based on this ground state, we derive in the Supplemental Material [30] the exact magnetostatic energy of the magnetized multidomain phase with a wall twist, $\sigma_d^{\infty,\mathcal{N}}(\lambda, W, \Delta, \psi_i)$ [Eq. (B1)]. We then derive expressions for the equilibrium domain parameters by minimizing the total energy $\mathcal{E}_{\text{tot}}^{\infty,\mathcal{N}}$ with respect to $\lambda, W, \Delta, \psi_i$ [see Eqs. (B6)–(B10)]. In Fig. 3(a) we plot W as a function of D for the demagnetized state ($\lambda = 2W$). We find that the full 3D treatment closely matches the 2D theory [22]. The largest deviation occurs for films with high Q and weak DMI and is caused by two effects: (i) surface-volume interactions, which are inherently ignored in the effective medium approach, and (ii) the intrinsic error of the effective medium approach [22], both of which have a comparable first-order effect on W. Note that the slope of the $W = W(D)$ curve approaches zero in the region of small DMI, which means that using domain width measurements for the extraction of small values of DMI is impractical.

IV. TWISTED SKYRMIONS

We next treat isolated skyrmions analytically using the wall-energy model [33], incorporating the twisted DW energy density derived above. Micromagnetic simulations reveal a layer-dependent radius R_i, which we plot in Fig. 3(b), for the case $f = 1/6$ with several values of Q and D (with fields B_z applied to yield similar radii). The skyrmion radius reaches a minimum at the top and the bottom layers and a maximum closer to the middle layer. This effect, similarly to the DW twist, is also caused by stray field interactions.

Since the interlayer variation of R_i and Δ_i is difficult to evaluate analytically, we approximate them as constant through the thickness (equal to R and Δ, respectively). Assuming that the DW energy is independent of R [valid for skyrmions with $R > \mathcal{O}(\Delta)$], we can express its total energy $E_{\text{tot}}^{\text{sk},\mathcal{N}}(R, \Delta, \psi_i, B_z)$ analogously to the 2D expression derived in Ref. [32], where the 3D twist is incorporated in the DW energy term:

$$E_{\text{tot}}^{\text{sk},\mathcal{N}} = 2\pi d R \sigma_{\text{tot}}^{1,\mathcal{N}} + aR - bR\ln(R/d) + cB_z R^2, \quad (9)$$

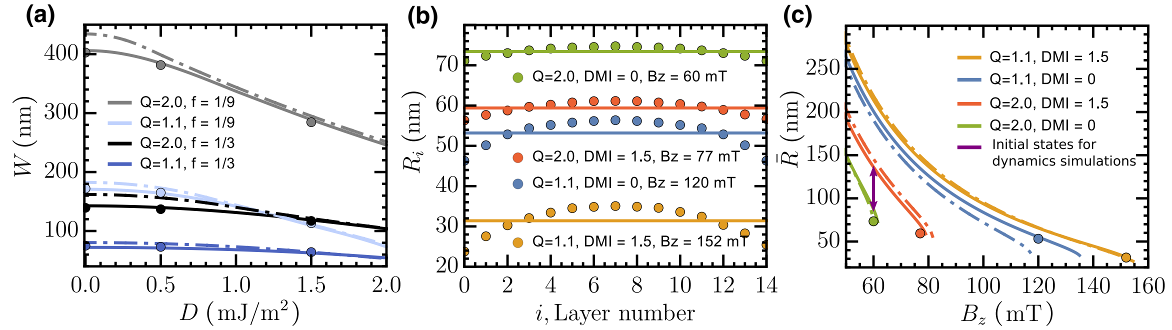

FIG. 3. Magnetic domains and skyrmions with twisted walls. (a) Equilibrium domain width as a function of interfacial DMI, Q and f. (b) R_i as a function of the layer number. (c) Average skyrmion radius $\sum_0^{\mathcal{N}-1} R_i/\mathcal{N}$ as a function of applied field, Q and D for films with $f = 1/6$. DMI constants D are in units of mJ/m^2. Solid (dashed) lines represent the numerical solution for 3D (2D [22,32]) theory, dots represent multilayer simulations, with explicit spacer layers.

where $\sigma_{\text{tot}}^{1,\mathcal{N}}(\Delta, \psi_i)$ is taken from Eq. (4), and constants are defined in Eqs. (C1)–(C4). The equilibrium R can be determined by simply plugging the equilibrium parameters Δ, ψ_i found from the straight DW theory [Eqs. (5) and (6)] into Eq. (9) and minimizing the resulting expression with respect to R. Note that skyrmions with topological charge $N = 1$ ($N = -1$) correspond to the lower (upper) sign in Eq. (6). We find that R predicted by our analytical theory is very close to the average R obtained from explicit multilayer simulations [Figs. 3(b) and 3(c)]. For comparison, the prediction of the 2D model derived in Ref. [32] [Fig. 3(c) applied by treating the multilayer using effective medium scaling] is seen to be quantitatively inaccurate due to the intrinsic error of the effective medium approach [17,22] and the ignored surface-volume stray field interactions.

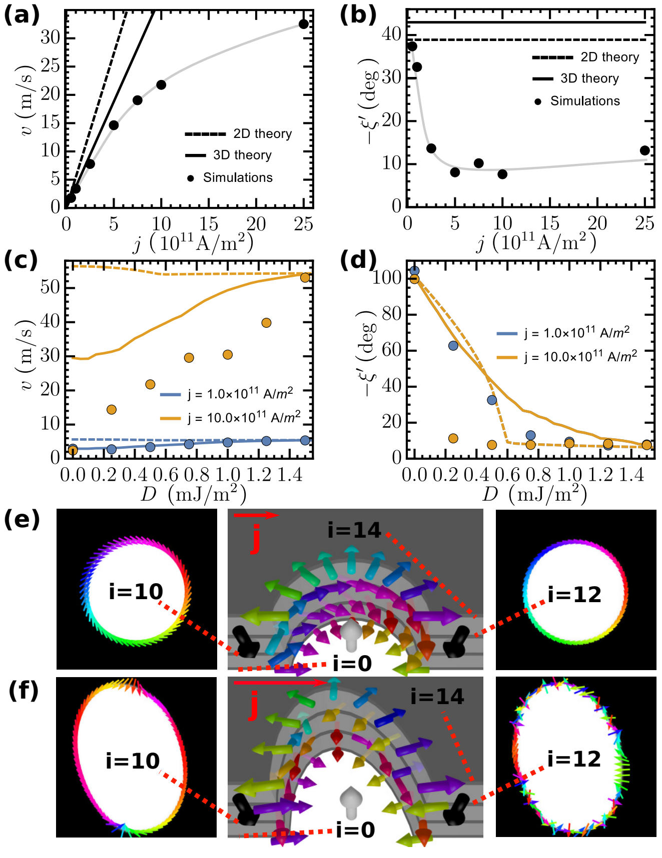

FIG. 4. Dynamics of skyrmions with twisted walls (a) Skyrmion velocity v and (b) skyrmion Hall angle ξ' as a function of current density j for films with $D = 0.5$ mJ/m^2 with gray continuous lines representing guides to the eye. (c) v and (d) ξ' as a function of DMI. Continuous (dotted) lines depict 3D (2D [32]) model. (e),(f) 3D cuts of multilayer skyrmions at $j = 1.0 \times 10^{11}$ A/m^2 and $j = 1.0 \times 10^{12}$ A/m^2 for films with $D = 0.5$ mJ/m^2 (at $t = 9$ ns). Simulation parameters are $Q = 2.0$, $f = 1/6$ (i.e., $D_{\text{thr}}^{3D} = 1.47$ mJ/m^2), $\theta_{\text{SH}} = 0.1$, $\alpha = 0.3$.

Finally, we examine current-induced dynamics of twisted skyrmions analytically and through micromagnetic simulations. For simplicity we consider only dampinglike spin-orbit torque (SOT). Treating the skyrmion as a rigid texture whose static configuration is preserved while moving, we use the Thiele equation [34] to derive analytical expressions for the steady state skyrmion velocity v and Hall angle ξ', similarly to the approach in Ref. [32]. By summing up the forces acting on each individual skyrmion in the multilayer, we arrive at [see Supplemental Material [30] and Eqs. (C5)–(C8)]:

$$|v| = j\frac{\pi\hbar\gamma\Delta\theta_{\text{SH}} I_D(\rho)}{2eM_s\mathcal{T}\sqrt{\tilde{G}^2 + \tilde{D}^2\alpha^2}}\tilde{f} \qquad (10)$$

$$\xi' = \text{atan2}(\tilde{\text{G}}, \tilde{\text{D}}\alpha) - (\tilde{\psi} - \pi/2) + \pi\Theta(\theta_{\text{SH}}\text{N}). \qquad (11)$$

The constants $\tilde{f}$, $\tilde{\psi}$ capture the influence of the DW twist:

$$\tilde{f} = \frac{1}{\mathcal{N}}\sqrt{\left(\sum_{i=0}^{\mathcal{N}-1}\cos(\psi_i)\right)^2 + \left(\sum_{i=0}^{\mathcal{N}-1}\sin(\psi_i)\right)^2} \qquad (12)$$

$$\tilde{\psi} = \text{atan2}\left(\sum_{\text{i}=0}^{\mathcal{N}-1}\sin(\psi_{\text{i}}), \sum_{\text{i}=0}^{\mathcal{N}-1}\cos(\psi_{\text{i}})\right). \qquad (13)$$

For the 2D model, these constants become $\tilde{f} = 1$ and $\tilde{\psi} = \psi_{\text{2D}}$ [32]. Hence, even if the 2D model could predict the equilibrium

R exactly, its predictions of skyrmion dynamics would still deviate from our multilayer treatment as $v_{3\mathrm{D}}/v_{2\mathrm{D}} = \tilde{f}$ and $\xi'_{3\mathrm{D}} - \xi'_{2\mathrm{D}} \equiv \tilde{\psi} - \psi_{2\mathrm{D}}$.

Figures 4(a) and 4(b) compare the values of v, ξ' predicted by these two theories, with the ones extracted from the explicit multilayer simulations for films with $f = 1/6$, $Q = 2.0$, $B_z = 59$ mT, $D = 0.5$ mJ/m^2. Both theories provide a reasonable estimate of the skyrmion Hall angle, however the velocity predictions in our 3D model are in much better agreement with the explicit multilayer simulations than are those of the 2D model [32], especially in the low current regime. The low-j deviations of ξ' in the 3D model are attributed to the slight underestimation of the ψ_i predicted by our model.

Micromagnetic simulations show that for small j, the skyrmion profile preserves its static configuration [Fig. 4(e)]. By contrast, at higher j, for some layers, ψ_i becomes nonuniform across the perimeter of the skyrmion, which leads to a reduced net force acting on the skyrmion tube. We generally find that the closer the static configuration in a layer is to being Bloch, the higher the likelihood that at high j the skyrmion in that layer accumulates pairs of Bloch lines [as depicted in Fig. 4(f)] and exhibits nonuniform precession and oscillations during current injection (as demonstrated for $D = 0.5$ mJ/m^2 in the Supplemental videos [30]). Both velocity and skyrmion Hall angle, particularly at high currents, are many times smaller than they would be in the absence of these factors, i.e., for the 2D model, or even for our (rigid) twisted wall-energy model [Figs. 4(a) and 4(b)]. These high-j phenomena affect the resulting dynamics of multilayer skyrmions, especially at low DMI. There, only a fraction of skyrmions contribute to the net force, since skyrmions in the upper and lower layers have opposite chiralities so that the forces tend to cancel. What is left are the transient and Bloch skyrmions that contribute only weakly due to the development of Bloch lines or wall angle oscillations [35], leading to significantly lower velocities. Such defects or oscillations are absent in layers with Néel walls, which is why our high-DMI predictions of v are always accurate [Figs. 4(c) and 4(d)]. Finally, we find that high currents also lead to distorted skyrmions shapes, as well as to their slight magnetostatic decoupling along the film. Such high-SOT effects may also contribute to the observed deviations of our 3D dynamics model.

V. SUMMARY

We have explicitly demonstrated that DWs and skyrmions in magnetic multilayers generally form a twisted structure with varying ψ_i Δ_i and R_i due to the mutual surface-volume stray field interactions. We have calculated the wall twist analytically, assuming a varying ψ_i, but a fixed $\Delta_i = \Delta$ across the layers. We have found that 2D treatments, in addition to completely ignoring the wall twist, yield quantitative errors in domain spacing and isolated skyrmion sizes, though in most cases the error is relatively modest. However, these twisted states, and the variation of the strength of stabilization of the DW angle through the thickness, leads to markedly different dynamics from what 2D treatments would predict. We derived analytical expressions for skyrmion velocity and Hall angle accounting for the twisted states, which work well at low current but fail at higher currents due to complex dynamical changes in the spin textures that cannot be captured by rigid models. Our work provides key insights into the novel static and dynamic layer-dependent phenomena in PMA multilayers.

ACKNOWLEDGMENTS

We thank Dr. Felix Büttner for optimizing the efficiency of the numerical script, providing the code templates to plot the figures and to extract the skyrmion parameters. This work was supported by the U.S. Department of Energy (DOE), Office of Science, Basic Energy Sciences (BES) under Award No. DE-SC0012371 (development of domain wall twist model) and by the DARPA TEE program (application to magnetic skyrmion statics and dynamics).

APPENDIX A: TWISTED STRAIGHT DOMAIN WALL

Films with layer dependent Δ_i, ψ_i exhibit an effective layer-dependent DMI, which stems from the surface-volume stray fields, and looks as follows (see Eq. S67 in the Supplemental Material [30])

$$D_{sv,i} = -\frac{2\mu_0 M_s^2 \Delta_i}{\mathcal{T}} \sum_{j=0}^{\mathcal{N}-1} \Delta_j \mathrm{sgn}(i-j) \int_0^\infty dk \frac{1}{k} \frac{e^{-k|(i-j)P+\mathcal{T}|} + e^{-k|(i-j)P-\mathcal{T}|} - 2e^{-k\mathcal{P}|i-j|}}{4\sinh\left(\frac{\pi\Delta_j k}{2}\right)\cosh\left(\frac{\pi\Delta_i k}{2}\right)}, \tag{A1}$$

which after a constant Δ assumption reduces to Eq. (8). The generic function $F_{\alpha,ij}$ used in the expression for the total magnetostatic energy of the isolated domain wall $\sigma_d^{1,\mathcal{N}}$ [Eq. (3)] is derived in the Supplemental Material [30] (Eqs. S35, S52, S69). It can be summarized as

$$F_{\alpha,ij}(\mathcal{T},\mathcal{P},\Delta) = \frac{\pi\mu_0 M_s^2\Delta^2}{\mathcal{N}\mathcal{P}}\left[G_\alpha\left(\frac{|(i-j)\mathcal{P}+\mathcal{T}|}{2\pi\Delta}\right) + G_\alpha\left(\frac{|(i-j)\mathcal{P}-\mathcal{T}|}{2\pi\Delta}\right) - 2G_\alpha\left(\frac{|(i-j)\mathcal{P}|}{2\pi\Delta}\right)\right] \tag{A2}$$

with functions $G_\alpha(x)$ defined analytically as follows:

$$G_v(x) = -2\left\{\Psi^{-2}(x+1) - \Psi^{-2}\left(x+\frac{1}{2}\right) - x\ \ln(\Gamma(x+1)) + x\ln\left[\Gamma\left(x+\frac{1}{2}\right)\right] - \Psi^{-2}(1) + \Psi^{-2}\left(\frac{1}{2}\right)\right\} \tag{A3}$$

$$G_s(x) = -\{\Psi^{(-2)}(2x) + x^2(2\log(x) + \log(4) - 1) - x(1 + 2\ln[\Gamma(2x)])\} \tag{A4}$$

$$G_{sv}(x) = 2\ln\left[\Gamma\left(x+\frac{1}{2}\right)\right], \tag{A5}$$

where the volume-volume stray field component $G_v(x)$ has been originally derived for homochiral multilayers in Ref. [36]. The value of DMI at which all the layers are saturated to the homochiral Néel state (D_{thr} [22]) can be derived from the following equations (with Δ_{thr} and D_{thr}^{3D} being the unknown variables).

$$2K_u f - \frac{2A}{\Delta_{\mathrm{thr}}^2} f + \sum_{i=0}^{\mathcal{N}-1}\sum_{j=0}^{\mathcal{N}-1}\left[\frac{\partial F_{s,ij}}{\partial \Delta_{\mathrm{thr}}} + \frac{\partial F_{v,ij}}{\partial \Delta_{\mathrm{thr}}} \pm \mathrm{sgn}(i-j)\frac{\partial F_{sv,ij}}{\partial \Delta_{\mathrm{thr}}}\right] = 0, \tag{A6}$$

$$\left(\sum_{j=0}^{\mathcal{N}-1}[(1+\delta_{ij})F_{v,ij}(\Delta_{\mathrm{thr}})]^{-1}\cdot\left[\frac{\pi D_{\mathrm{thr}}^{3D} f}{\mathcal{N}}1_j - \sum_{k=0}^{\mathcal{N}-1} F_{sv,jk}(\Delta_{\mathrm{thr}})\mathrm{sgn}(j-k)\right]\right)_{\mathcal{N}-1} - 1 = 0, \tag{A7}$$

where the sign "-1" represents the matrix inversion operation. This value can be compared with the value given by the 2D model [22], extending it to multilayers via the effective medium approach [17,21,22]:

$$D_{\mathrm{thr}}^{2D} = \frac{2\mu_0 M_s^2 f}{\frac{\pi^2}{\mathcal{P}\mathcal{N}\ln(2)} + \pi\sqrt{\frac{K_u - \frac{\mu_0 M_s^2}{2} + \mu_0 M_s^2 f}{A}}}. \tag{A8}$$

APPENDIX B: DOMAIN SIZE

The total magnetostatic energy of magnetized multidomain multilayers is derived in the Supplemental Material [30] (Eqs. S101, S118, S130) and can be expressed as

$$\begin{aligned}\sigma_d^{\infty,\mathcal{N}} &= \frac{\lambda}{4}\mu_0 M_s^2\left(\frac{2W}{\lambda}-1\right)^2\frac{\mathcal{T}}{\mathcal{P}} + \sum_{i=0}^{\mathcal{N}-1}\sum_{j=0}^{\mathcal{N}-1}\tilde{F}_{s,ij}(\mathcal{T},\mathcal{P},\Delta,\lambda,W)\\ &\quad + \sum_{i=0}^{\mathcal{N}-1}\sum_{j=0}^{\mathcal{N}-1}\{\sin(\psi_i)\sin(\psi_j)\tilde{F}_{v,ij}(\mathcal{T},\mathcal{P},\Delta,\lambda,W) + \sin(\psi_i)\mathrm{sgn}(i-j)\tilde{F}_{sv,ij}(\mathcal{T},\mathcal{P},\Delta,\lambda,W)\}\end{aligned} \tag{B1}$$

with a generic function $\tilde{F}_{\alpha,ij}$ and its dependencies defined as follows

$$\tilde{F}_{\alpha,ij} = \frac{\pi\mu_0 M_s^2\Delta^2}{\mathcal{N}\mathcal{P}}\sum_{n=1}^{\infty}\frac{\sin^2\left(\frac{\pi n W}{\lambda}\right)}{n}\tilde{G}_{\alpha,ijn}(\mathcal{T},\mathcal{P},\Delta,\lambda), \tag{B2}$$

$$\tilde{G}_{v,ijn} = \frac{2\sinh^2\left(\frac{\pi n\mathcal{T}}{\lambda}\right)e^{-\frac{2\pi n\mathcal{P}|i-j|}{\lambda}}(1-\delta_{ij}) + \left(e^{-\frac{2\pi n\mathcal{T}}{\lambda}} + \frac{2\pi n\mathcal{T}}{\lambda} - 1\right)\delta_{ij}}{\cosh^2\left(\frac{\pi^2 n\Delta}{\lambda}\right)} \tag{B3}$$

$$\tilde{G}_{s,ijn} = \frac{2e^{-\frac{2\pi|(i-j)\mathcal{P}|n}{\lambda}} - e^{-\frac{2\pi|\mathcal{T}-(i-j)\mathcal{P}|n}{\lambda}} - e^{-\frac{2\pi|\mathcal{T}+(i-j)\mathcal{P}|n}{\lambda}}}{2\sinh^2\left(\frac{\pi^2 n\Delta}{\lambda}\right)} \tag{B4}$$

$$\tilde{G}_{sv,ijn} = \frac{8\sinh^2\left(\frac{\pi n\mathcal{T}}{\lambda}\right)e^{-\frac{2\pi n\mathcal{P}|i-j|}{\lambda}}}{\sinh\left(\frac{2\pi^2 n\Delta}{\lambda}\right)}. \tag{B5}$$

Assuming the magnetic field applied in the z direction (in the absence of currents), the total volumetric energy per single domain wall per layer therefore can be expressed as:

$$\mathcal{E}_{\mathrm{tot}}^{\infty,\mathcal{N}}(\lambda,W,\Delta,\psi_i) = \frac{2}{\lambda}\left[\frac{2A}{\Delta}f + 2K_u\Delta f - M_s\left(1-\frac{2W}{\lambda}\right)B_z\frac{f\lambda}{2} + \sigma_d^{\infty,\mathcal{N}}(\lambda,W,\Delta,\psi_i) - \frac{\pi D f}{\mathcal{N}}\sum_{i=0}^{\mathcal{N}-1}\sin(\psi_i)\right]. \tag{B6}$$

By performing the energy minimization (as shown in the Supplemental Material [30]), we will have the system of four equations that define the equilibrium λ, W, Δ, ψ:

$$\begin{aligned}&\sum_{i=0}^{\mathcal{N}-1}\sum_{j=0}^{\mathcal{N}-1}\left\{\left[\tilde{F}_{s,ij} - \lambda\frac{\partial\tilde{F}_{s,ij}}{\partial\lambda}\right] + \sin(\psi_i)\sin(\psi_j)\left[\tilde{F}_{v,ij} - \lambda\frac{\partial\tilde{F}_{v,ij}}{\partial\lambda}\right] + \sin(\psi_i)\mathrm{sgn}(i-j)\left[\tilde{F}_{sv,ij} - \lambda\frac{\partial\tilde{F}_{sv,ij}}{\partial\lambda}\right]\right\}\\ &\quad + \left[\frac{2A}{\Delta}f + 2K_u\Delta f - \frac{\pi D f}{\mathcal{N}}\sum_{i=0}^{\mathcal{N}-1}\sin(\psi_i) + W M_s B_z f + \mu_0 M_s^2 W f\left(\frac{2W}{\lambda}-1\right)\right] = 0,\end{aligned} \tag{B7}$$

$$M_s f\left[B_z + \mu_0 M_s\left(\frac{2W}{\lambda}-1\right)\right] + \sum_{i=0}^{\mathcal{N}-1}\sum_{j=0}^{\mathcal{N}-1}\left\{\frac{\partial\tilde{F}_{s,ij}}{\partial W} + \sin(\psi_i)\sin(\psi_j)\frac{\partial\tilde{F}_{v,ij}}{\partial W} + \sin(\psi_i)\mathrm{sgn}(i-j)\frac{\partial\tilde{F}_{sv,ij}}{\partial W}\right\} = 0, \tag{B8}$$

$$-\frac{2A}{\Delta^2}f + 2K_u f + \sum_{i=0}^{\mathcal{N}-1}\sum_{j=0}^{\mathcal{N}-1}\frac{\partial \tilde{F}_{s,ij}}{\partial \Delta} + \sum_{i=0}^{\mathcal{N}-1}\sum_{j=0}^{\mathcal{N}-1}\sin(\psi_i)\sin(\psi_j)\frac{\partial \tilde{F}_{v,ij}}{\partial \Delta} + \sum_{i=0}^{\mathcal{N}-1}\sum_{j=0}^{\mathcal{N}-1}\sin(\psi_i)\mathrm{sgn}(i-j)\frac{\partial \tilde{F}_{sv,ij}}{\partial \Delta} = 0, \tag{B9}$$

$$\sin(\psi_i) = \tilde{f}\left(\sum_{j=0}^{\mathcal{N}-1}[(1+\delta_{ij})\tilde{F}_{v,ij}(\Delta, W)]^{-1}\left[\frac{\pi D f}{\mathcal{N}}1_j - \sum_{k=0}^{\mathcal{N}-1}\tilde{F}_{sv,jk}(\Delta, W)\mathrm{sgn}(j-k)\right]\right), \tag{B10}$$

where the sign "$^{-1}$" represents the matrix inversion operation.

APPENDIX C: TWISTED SKYRMIONS

For the skyrmion statics expressions [Eq. (9) and Eq. (S150)], we have used the constants defined in the Supplemental Material [30] and Ref. [32] as:

$$a = -\mu_0 M_s^2(\mathcal{P}\mathcal{N})^2[6\ln(2) - 1] \tag{C1}$$

$$b = 2\mu_0 M_s^2(\mathcal{P}\mathcal{N})^2 \tag{C2}$$

$$c = -2\pi\mathcal{P}\mathcal{N}M_s \tag{C3}$$

$$d = \mathcal{P}\mathcal{N}. \tag{C4}$$

Similarly, the constants for the skyrmion dynamics [Eqs. (10) and (11)] are [32]

$$\tilde{G} = -4\pi N \tag{C5}$$

$$\tilde{D} = \pi I_A(R/\Delta) \tag{C6}$$

$$I_{\mathrm{A}}(\rho) = 2\rho + \frac{2}{\rho} + 1.93(\rho - 0.65)\exp[-1.48(\rho - 0.65)] \tag{C7}$$

$$I_{\mathrm{D}}(\rho) = \pi\rho + \frac{1}{2}\exp(-\rho). \tag{C8}$$

APPENDIX D: METHODS

For simulating magnetic textures (isolated domain walls, perpendicular stripes, and skyrmions), the micromagnetic MuMax3 solver [37] was used with the magnetic parameters given in the paper. The cell size is 1 nm × 1 nm × 1 nm and the simulation size is 1 μm × 1 μm × $\mathcal{N}\mathcal{P}$. For skyrmion dynamics simulations, Zhang-Li torque has been disabled, and the modified Slonczewski-like torque module has been used (with the dampinglike torque enabled and fieldlike torque disabled). Spin Hall angle is $\Theta_{\mathrm{SH}} = 0.1$, damping constant $\alpha = 0.3$; fixed layer polarization is along the $-y$ direction.

[1] M. Heide, G. Bihlmayer, and S. Blügel, Phys. Rev. B **78**, 140403 (2008).

[2] A. Thiaville, S. Rohart, É. Jué, V. Cros, and A. Fert, EPL **100**, 57002 (2012).

[3] S. Emori, U. Bauer, S. M. Ahn, E. Martinez, and G. S. D. Beach, Nat. Mater. **12**, 611 (2013).

[4] U. K. Rößler, A. N. Bogdanov, and C. Pfleiderer, Nature (London) **442**, 797 (2006).

[5] S. Mühlbauer, B. Binz, F. Jonietz, C. Pfleiderer, A. Rosch, A. Neubauer, R. Georgii, and P. Böni, Science **323**, 915 (2009).

[6] A. Fert, V. Cros, and J. Sampaio, Nat. Nanotechnol. **8**, 152 (2013).

[7] F. N. Rybakov, A. B. Borisov, and A. N. Bogdanov, Phys. Rev. B **87**, 094424 (2013).

[8] S. A. Meynell, M. N. Wilson, H. Fritzsche, A. N. Bogdanov, and T. L. Monchesky, Phys. Rev. B **90**, 014406 (2014).

[9] A. O. Leonov, Y. Togawa, T. L. Monchesky, A. N. Bogdanov, J. Kishine, Y. Kousaka, M. Miyagawa, T. Koyama, J. Akimitsu, T. Koyama, K. Harada, S. Mori, D. McGrouther, R. Lamb, M. Krajnak, S. McVitie, R. L. Stamps, and K. Inoue, Phys. Rev. Lett. **117**, 087202 (2016).

[10] F. N. Rybakov, A. B. Borisov, S. Blügel, and N. S. Kiselev, New J. Phys. **18**, 045002 (2016).

[11] D. McGrouther, R. J. Lamb, M. Krajnak, S. McFadzean, S. McVitie, R. L. Stamps, A. O. Leonov, A. N. Bogdanov, and Y. Togawa, New J. Phys. **18**, 095004 (2016).

[12] S. L. Zhang, G. van der Laan, W. W. Wang, A. A. Haghighirad, and T. Hesjedal, Phys. Rev. Lett. **120**, 227202 (2018).

[13] Y. Yoshida, S. Schroder, P. Ferriani, D. Serrate, A. Kubetzka, K. von Bergmann, S. Heinze, and R. Wiesendanger, Phys. Rev. Lett. **108**, 087205 (2012).

[14] N. Romming, A. Kubetzka, C. Hanneken, K. von Bergmann, and R. Wiesendanger, Phys. Rev. Lett. **114**, 177203 (2015).

[15] R. Wiesendanger, Nat. Rev. Mater. **1**, 16044 (2016).

[16] F. Büttner, C. Moutafis, M. Schneider, B. Krüger, C. M. Günther,

J. Geilhufe, C. V. K. Schmising, J. Mohanty, B. Pfau, S. Schaffert, A. Bisig, M. Foerster, T. Schulz, C. A. F. Vaz, J. H. Franken, H. J. M. Swagten, M. Kläui, and S. Eisebitt, Nat. Phys. **11**, 225 (2015).

[17] S. Woo, K. Litzius, B. Krüger, M.-Y. Im, L. Caretta, K. Richter, M. Mann, A. Krone, R. M. Reeve, M. Weigand, P. Agrawal, I. Lemesh, M.-A. Mawass, P. Fischer, M. Kläui, and G. S. D. Beach, Nat. Mater. **15**, 501 (2016).

[18] C. Moreau-Luchaire, C. Moutafis, N. Reyren, J. Sampaio, C. A. Vaz, N. Van Horne, K. Bouzehouane, K. Garcia, C. Deranlot, P. Warnicke, P. Wohlhüter, J. M. George, M. Weigand, J. Raabe, V. Cros, and A. Fert, Nat. Nanotechnol. **11**, 444 (2016).

[19] K. Litzius, I. Lemesh, B. Krüger, L. Caretta, K. Richter, F. Büttner, P. Bassirian, J. Förster, R. M. Reeve, M. Weigand, I. Bykova, H. Stoll, G. Schütz, G. S. D. Beach, and M. Kläui, Nat. Phys. **13**, 170 (2016).

[20] F. Büttner, I. Lemesh, M. Schneider, B. Pfau, C. M. Günther, P. Hessing, J. Geilhufe, L. Caretta, D. Engel, B. Krüger, J. Viefhaus, S. Eisebitt, and G. S. D. Beach, Nat. Nanotechnol. **12**, 1040 (2017).

[21] A. Suna, J. Appl. Phys. **59**, 313 (1986).

[22] I. Lemesh, F. Büttner, and G. S. D. Beach, Phys. Rev. B **95**, 174423 (2017).

[23] Y. Dovzhenko, F. Casola, S. Schlotter, T. X. Zhou, F. Büttner, R. L. Walsworth, G. S. D. Beach, and A. Yacoby, Nat. Commun. **9**, 2712 (2018).

[24] S. A. Montoya, S. Couture, J. J. Chess, J. C..T Lee, N. Kent, D. Henze, S. K. Sinha, M. Y. Im, S. D. Kevan, P. Fischer, B. J. McMorran, V. Lomakin, S. Roy, and E. E. Fullerton, Phys. Rev. B **95**, 024415 (2017).

[25] E. Schlömann, J. Appl. Phys. **44**, 1837 (1973).

[26] E. Schlömann, J. Appl. Phys. **44**, 1850 (1973).

[27] In our notations, $\sigma^{\mathcal{M},\mathcal{N}}$ indicates the energy (per multilayer cross section) of $\mathcal{M}$ DWs in the film with $\mathcal{N}$ multilayer repeats.

[28] Our approximation assumes that $\mathcal{T} < l_{\mathrm{ex}}$.

[29] W. Legrand, J.-Y. Chauleau, D. Maccariello, N. Reyren, S. Collin, K. Bouzehouane, N. Jaouen, V. Cros, and A. Fert, Sci. Adv. **4**, eaat0415 (2018).

[30] See Supplemental Material at http://link.aps.org/supplemental/10.1103/PhysRevB.98.104402 for the detailed derivation of energetics of twisted domain walls, domains, and skyrmions in PMA multilayers and videos which demonstrate the dynamic accumulation of Bloch line pairs in twisted skyrmions in high-j regime (with $j = 1.0 \times 10^{12}\mathrm{j/m^2}$, spin Hall angle 0.1, $D = 0.5\ \mathrm{mJ/m^2}$, $\alpha = 0.3$, and $B_z = 59$ mT).

[31] S. Rohart and A. Thiaville, Phys. Rev. B **88**, 184422 (2013).

[32] F. Büttner, I. Lemesh, and G. S. D. Beach, Sci. Rep. **8**, 1 (2018).

[33] J. A. Cape and G. W. Lehman, J. Appl. Phys. **42**, 5732 (1971).

[34] A. A. Thiele, Phys. Rev. Lett. **30**, 230 (1973).

[35] A. Malozemoff and J. Slonczewski, *Magnetic Domain Walls in Bubble Materials* (Academic Press, New York, 1979), pp. 149–152.

[36] F. Büttner, B. Krüger, S. Eisebitt, and M. Kläui, Phys. Rev. B **92**, 054408 (2015).

[37] A. Vansteenkiste, J. Leliaert, M. Dvornik, M. Helsen, F. Garcia-Sanchez, and B. Van Waeyenberge, AIP Advances **4**, 107133 (2014).